

## REVIEW

[View Article Online](#)  
[View Journal](#) | [View Issue](#)



Cite this: *Biomater. Sci.*, 2024, **12**, 1357

## Renal-clearable nanoprobes for optical imaging and early diagnosis of diseases

Wei An,<sup>a,c</sup> Weiping Xu,<sup>b</sup> Ya Zhou,<sup>b</sup> Changwen Huang,<sup>d</sup> Weiguo Huang  \*<sup>a,c</sup> and Jiaguo Huang  <sup>b\*</sup><sup>b</sup>

Optical imaging has played an indispensable role in clinical diagnostics and fundamental biomedical research due to its high sensitivity, high spatiotemporal resolution, cost-effectiveness, and easy accessibility. However, the issues of light scattering and low tissue penetration make them effective only for superficial imaging. To overcome these issues, renal-clearable optical nanoprobes have recently emerged, which are activated by abnormal disease-associated biomarkers and initiate a pharmacokinetic switch by undergoing degradation and eventually releasing signal reporters into urine, for simple imaging and sensitive optical *in vitro* urinalysis. In this review, we focus on the advancements of renal-clearable organic nanoprobes for optical imaging and remote urinalysis. The versatile design strategies of these nanoprobes are discussed along with their sensing mechanisms toward biomolecules of interest as well as their unique biological applications. Finally, challenges and perspectives are discussed to further advance the next-generation renal-clearable nanoprobes for *in vivo* imaging and *in vitro* urinalysis.

Received 31st October 2023,  
Accepted 6th February 2024  
DOI: 10.1039/d3bm01776a  
[rsc.li/biomaterials-science](http://rsc.li/biomaterials-science)

## 1. Introduction

Molecular imaging enables non-invasive and real-time visualization of physiological or pathological processes in living

organisms.<sup>1–3</sup> With the combination of specialized instruments and imaging probes that reflect imaging signals, molecular imaging has played significant roles in early diagnosis, proper disease management, and drug development and discovery.<sup>4–7</sup> Several imaging modalities such as X-ray computed tomography (CT) imaging, positron emission tomography (PET), single-photon emission computerized tomography (SPECT), magnetic resonance imaging (MRI) and ultrasound (US) imaging are employed for deep tissue imaging in clinical practice.<sup>8–11</sup> Unlike those conventional imaging modalities, optical imaging as a nonionizing radiation method offers unique opportunities to real-time visualize and quantify mul-

<sup>a</sup>State Key Laboratory of Structural Chemistry, Fujian Institute of Research on the Structure of Matter, Chinese Academy of Sciences, Fuzhou, Fujian, 350002, China

<sup>b</sup>Department School of Pharmaceutical Sciences, Sun Yat-sen University, Guangzhou, 510006, China. E-mail: huangjg36@mail.sysu.edu.cn

<sup>c</sup>University of Chinese Academy of Sciences, Beijing 100049, P. R. China

<sup>d</sup>General surgery department, the Sixth Affiliated Hospital of Guangzhou Medical University, Qingyuan People's Hospital, Qingyuan, Guangdong, 511518, China



Wei An

Wei An graduated in 2021 with a bachelor's degree in Polymer Materials and Engineering from North University of China. Currently, she is pursuing a master's degree under the supervision of Professor Weiguo Huang at the University of Chinese Academy of Sciences. Her primary research focus lies in the design of stimuli-responsive polymer materials and the synthesis of platinum-based drugs, with a particular emphasis on their applications in biomedicine.



Weiping Xu

Weiping Xu received his Ph.D. from Guangdong University of Technology in 2022. Then he joined Prof. Jiaguo Huang's group at the School of Pharmaceutical Sciences, Sun Yat-Sen University and worked as a postdoctoral fellow. His current research interests are focused on novel small molecular probes for *in vivo* imaging and disease diagnosis.

tiple dynamic biological events at the molecular level with high spatiotemporal resolution and high sensitivity.<sup>12–17</sup> To correlate the signal with biomolecules or biological events *in vivo*, optical probes are of high significance. In clinical settings, imaging-guided surgery with clinically approved indocyanine green (ICG) and methylene blue (MB) have been widely investigated.<sup>18,19</sup> Moreover, renal-clearable small molecular probes have been explored to detect versatile pathological parameters in kidney disease, bladder cancer, cancer immunotherapy, etc.<sup>20–22</sup> However, these small molecular fluorophores typically experienced short retention time because of their rapid clearance.<sup>23,24</sup> In contrast, optical nanoparticulate probes with prolonged circulation time and biomarker-triggered signals offer measurable and quantifiable real-time information on pathological status at the molecular level.<sup>25,26</sup> Nevertheless, nanoprobes combined with optical imaging often encounter the shallow tissue penetration depth due to high photon absorption and scattering, which hampers imaging invisible or deep tissue diseases.<sup>27–29</sup>

Nanoparticles could disassemble or degrade into small molecules with desired properties such as fluorescence turn on and renal clearance in the presence of biomarkers of interest, which not only offer measurable real-time information on pathological sites but also leverage the level of biomarkers to amplify the detection signals in urine, allowing highly sensitive detection of diseases.<sup>30</sup> Thus far, only few nanoprobes built on metal materials such as gold nanoclusters have been reported for this purpose.<sup>31</sup> However, the design of those inorganic nanoprobes simply relies on the surface anchor *via* noncovalent bonds and the use of heavy metals failed to thoroughly be degraded.<sup>32</sup> Moreover, the *in vivo* stability and long-term biosafety remain to be optimized. By contrast, organic nanoprobes are more biocompatible, show faster clearance and have more tunable optical properties relative to inorganic nanomaterials. As most organic dye-based nanoparticles have been constructed through intraparticle doping, they are often unable to disassemble upon exposure to biological events, or their disassembled fragments failed to clear into urine. Therefore, organic nanoprobes that simultaneously

possess activatable fluorogenic signals and undergo degradation into small molecules with high renal clearance efficiency are promising for both real-time optical imaging *in vivo* and urinalysis *in vitro*.

The publications and citations about optical nanoprobes are increasing in number, and there are some reviews summarizing their designs, optical properties, and general biosensing applications. However, the existing literature has showcased the design strategies and therapeutic prospects of optical nanoprobes, which are mostly excreted through hepatobiliary clearance pathway. In this review, we focus on the recent progress in the development of renal-clearable organic nanoprobes for optical imaging and urinalysis and highlight the nanoprobe design and sensing mechanisms toward biomolecules or biological events of interest (Table 1). In the following sections, we first discuss the design principles of renal clearable nanoprobes along with their biological applications towards various conditions including cancers, allograft rejection, immunotherapy, infection, and thrombosis (Fig. 1). Furthermore, we discuss the challenges that exist in this growing field in the setting of preclinical studies and strategies for clinical translation.

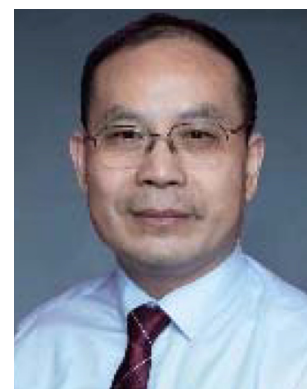
## 2. Early detection of cancer and acute allograft rejection

Cancer is a leading cause of disease-related death worldwide.<sup>4</sup> Early diagnosis plays a crucial role in the timely identification of cancers or precancerous lesions, enabling interventions that can enhance survival rates and reduce incidence. Conventional clinical radiological imaging modalities have limitations in detecting cancers at an early stage.<sup>4</sup> Moreover, solid organ transplantation is the only option for patients with end-stage cancer. However, acute allograft rejection manifests as a sudden decline in graft function after transplantation and poses a serious medical complication with high mortality risk in clinical settings. Therefore, early detection of allograft rejection is critical for long-term graft function and survival in transplant patients.



**Ya Zhou**

Ya Zhou is a PhD candidate in Sun Yat-sen University from 2021, under the supervision of Professor Jiaguo Huang. She received her Master of Medicine degree in pharmacology in 2020 and Bachelor of Science degree in pharmaceutical analysis in 2017, currently focuses on molecular probe imaging-related research, particularly on molecular pharmacology and urinalysis.



**Changwen Huang**

Changwen Huang received his PhD degree from Nanchang University in 2009. Since 2022, he has joined into general surgery department, the Sixth Affiliated Hospital of Guangzhou Medical University. His research interests include the pathology of hepatobiliary and pancreatic neoplasms and the basis of hepatobiliary and pancreatic surgery.

**Table 1** Summary of renal-clearable organic nanoprobes and their applications

Disease type	Probe	Biomarkers	Application	Ref.
Cancer	APN <sub>C</sub>	Cathepsin B	NIRF imaging in orthotopic liver tumour model and urinalysis <i>in vitro</i>	33
	ABN <sub>S</sub>	MMP9	Imaging in tumour nodules and urinalysis <i>in vitro</i>	36
	APN <sub>G</sub>	Granzyme B	Urinalysis in orthotopic liver transplantation of rat model	33
Allograft rejection				
Immunotherapy	$\alpha$ PD1-GS	Granzyme B	Urinalysis in MC38 colon adenocarcinoma syngeneic tumour model and Imaging in tumour organs	44
Thrombosis	PEG-T1E	Thrombin	ELISA and paper ELISA	60
Inflammation	PEG-M1E	MMP9	ELISA and paper ELISA	60
Hepatic IRI	APN <sub>SO</sub>	O <sub>2</sub> <sup>·-</sup>	Detecting O <sub>2</sub> <sup>·-</sup> , NIRF imaging and urinalysis	55
DILI	ADN2	O <sub>2</sub> <sup>·-</sup>	Detecting O <sub>2</sub> <sup>·-</sup> , NIRF imaging and urinalysis	63

MMP9: matrix metalloproteinase-9, Hepatic IRI: hepatic ischemia-reperfusion injury, DILI: drug-induced liver injury, O<sub>2</sub><sup>·-</sup>: superoxide anion.

Although invasive biopsy is the gold standard routinely used to diagnose allograft rejection, this procedure is invasive and offers only a static and focal pathological state.<sup>33</sup>

To overcome these issues, Pu and his colleagues have reported activatable polyfluorescent nanoprobes (APNs) for real-time near-infrared fluorescence (NIRF) imaging and urinalysis of tumours and allograft rejection.<sup>33</sup> These APNs consist of fluorophores with azide groups incorporated into alkyl chains (NH<sub>2</sub>CyOH), along with an aniline group linked to a self-immolative linker (4-aminophenyl conjugated benzoyldimethanol) (Fig. 2b). This self-immolative linker is employed in conjunction with dipeptide acetyl-Phe-Lys (Ac-FK) or tetrapeptide acetyl-Ile-Glu-Phe-Asp (Ac-IEFD), resulting in the formation of polymer C and polymer G (Fig. 2a). To enhance their hydrophilicity and targeting ability, the azide groups on the side chains of polymer C/G are further coupled with cRGDFK/HP $\beta$ CD or HP $\beta$ CD, affording APN<sub>C</sub> and APN<sub>G</sub>, respectively.<sup>34,35</sup> It should be noted that Ac-FK and Ac-IEFD peptide moieties can be specifically cleaved by Cathepsin B (Cat B) and Granzyme B (GzmB) proteases, respectively, which are highly expressed in tumour cells and lymphocyte cells during allograft rejection, respectively.



Weiguo Huang

*emission (DETE), biochemical sensors, organic electro-optics and photonics, and soft smart matter.*

The amphiphilicity of APN<sub>C</sub> and APN<sub>G</sub> enabled spontaneous assembly into spherical nanoparticles with average dynamic sizes of ~170 nm. APN<sub>C</sub> and APN<sub>G</sub> are naturally non-fluorescent in PBS solutions. After incubation with cathepsin B and granzyme B, the fluorescence at 720 nm increased by 11-fold and 10-fold (Fig. 2c and 3b) for APN<sub>C</sub> and APN<sub>G</sub>, respectively. This was attributed to the enzymatic cleavage of the amide linkage between the peptide substrate and the self-immolative moiety, followed by 1,6-elimination and 1,4-elimination, eventually leading to depolymerization to form fluorescent CyCD or CyRGD. Moreover, their sizes decreased dramatically upon incubation with respective proteases, as they underwent backbone degradation and thus stayed in a single-molecule state rather than nanoparticle state in aqueous solutions.

Owing to the size of APNs (~170 nm) being far over the renal filtration threshold (~5 nm) and intrinsic non-fluorescent feature, APNs accumulated predominately in the liver and showed weak fluorescence. After systematic injection into live mice carrying an orthotopic liver tumour in a mouse model, the tumour in the liver was easily delineated through NIRF imaging. Meanwhile, the fluorescence signal was



Jiaguo Huang

*real-time *in vivo* imaging and detection of life-threatening diseases.*

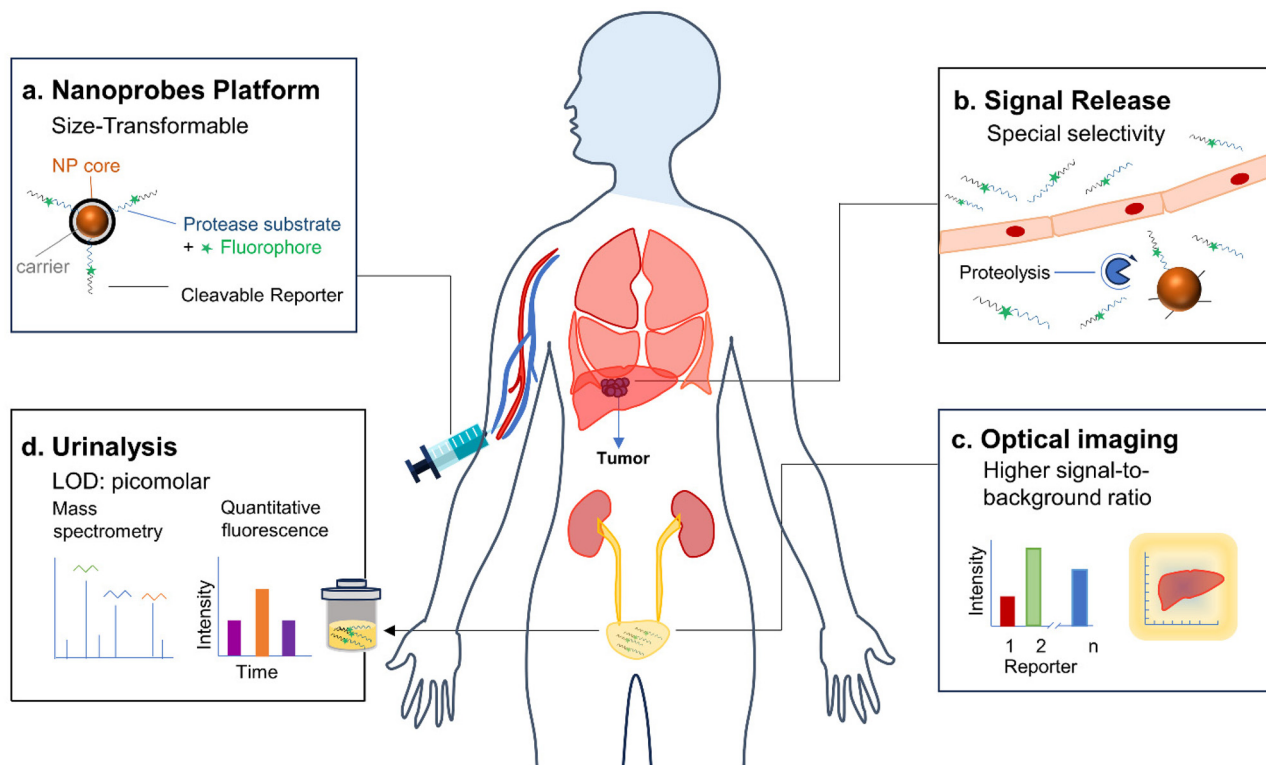
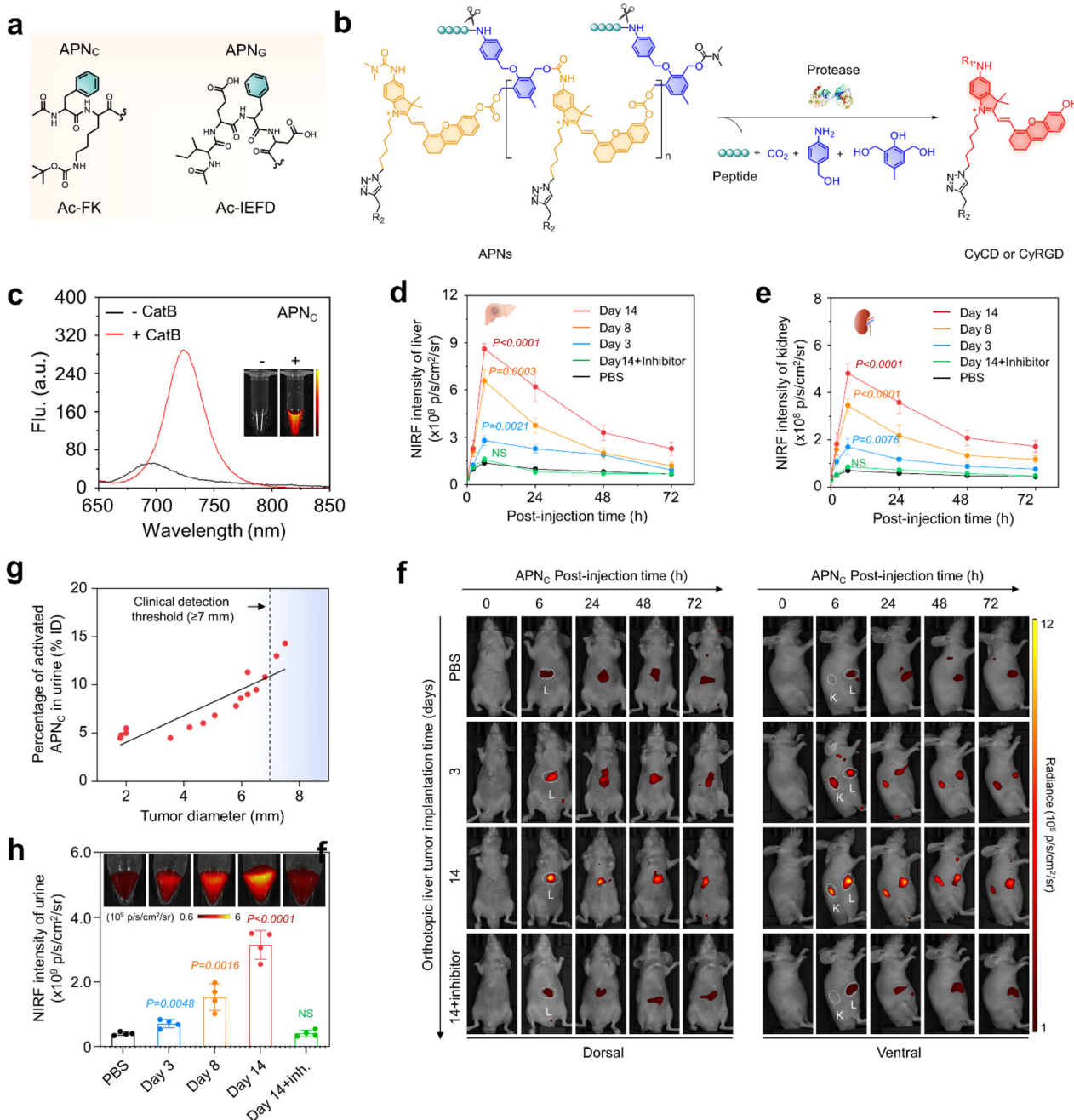


Fig. 1 Schematic illustration of the applications of renal-clearable nanoprobes for imaging and urinalysis of diseases.

detected in the kidneys (Fig. 2f), because the overexpressed cathepsin B in the tumour effectively activated APN<sub>C</sub>, leading to depolymerization to produce fluorescent artificial urinary biomarker CyCD with a strong fluorescence signal. The maximum liver-to-background ratio (LBR) and kidney-to-background ratio (KBR) were 5.6-fold and 6.9-fold higher than those of the control mice, respectively (Fig. 2d and e). A gradual decline in these ratios was observed at later time points due to the renal clearance of CyCD. Furthermore, a separate cohort of tumour-bearing mice were treated with a cathepsin B inhibitor (CA-074) prior to APN<sub>C</sub> administration. Pharmacological inhibition of cathepsin B resulted in a remarkable decrease in signal for both liver and kidneys.

The intra-tumour Cathepsin B levels was detected by urinalysis of the CyCD signal following APN<sub>C</sub> injection. On days 3, 8, and 14 after tumour implantation, the intra-tumour Cathepsin B levels gradually increased, corresponding to CyCD signal increases of 1.8-fold, 3.8-fold, and 7.8-fold, respectively, in comparison to control mice (Fig. 2h). Notably, the percentage of activated APN<sub>C</sub> in urine closely correlated with the tumour size. APN<sub>C</sub>-based urinalysis demonstrated its capability to *in situ* detect liver tumours as small as approximately 1.9 mm in diameter, outperforming the conventional clinical liver function tests including glutamate transaminase (ALT) and aspartate transaminase (AST) (Fig. 2g). Hence, it is anticipated that APN<sub>C</sub> are superior to conventional clinical assays for the early diagnosis of liver cancer.

In an orthotopic liver transplantation of rat model (Fig. 3a), APN<sub>G</sub> was i.v. injected into live rats at different post-operation time points (2, 3, 4 and 6 days). Urinalysis was conducted and their signals were normalized by the fold of urinary protein in order to exclude the effect of urine volume between different rats. The first statistically significant NIRF enhancement for excreted CyCD was observed at 3 days (3.2-fold) post operation, which continued to increase to 4.9-fold at 4 days and 3.9-fold at 6 days post operation. Moreover, there was no significant elevation in urine signals from high-dose tacrolimus-treated grafted rats, iso-grafted rats and sham-operated rats with only trauma on the belly. The signal evolution behaviors of urinalysis coincided well with the level of granzyme B in CD8+ cytotoxic T cells from liver, spleen, lymph nodes and blood by flow cytometry. Moreover, the sensitivity and specificity for all tested assays including APN<sub>G</sub>-based urinalysis, flow cytometry, cytokines and liver function were evaluated (Fig. 3c and d). Different from the limited predictive power of cytokines for early detection ( $0.69 < \text{AUC} < 0.91$ ), APN<sub>G</sub>-based urinalysis and flow cytometry assays were highly discriminatory, producing a higher AUC ( $0.94 < \text{AUC} < 0.98$ ). Although ALT and AST had a comparable predictive power ( $\text{AUC} = 0.96$  and  $0.98$ ), their detection time was delayed to 4 days post operation time. Therefore, APN<sub>G</sub>-based urinalysis not only enabled the detection of allograft rejection early, but also showed the highest sensitivity to in the prediction and prognosis of acute liver allograft rejection.



**Fig. 2** NIRF imaging and urinalysis of APN<sub>c</sub> for early cancer diagnosis. (a) Chemical structures of protease-responsive peptide brushes (Ac-FK and Ac-IEFD) for APN<sub>s</sub> design. (b) Chemical structures of APN<sub>s</sub> and the corresponding fluorogenic fragments in response to the respective proteases (CyCD or CyRGD). (R<sub>1</sub> = H or (CH<sub>3</sub>)<sub>2</sub>NCO, R<sub>2</sub> = HPβCD or cRGD, R<sub>3</sub> = H or CH<sub>2</sub>CHOHCH<sub>3</sub>). (c) NIR-fluorescence spectra of APN<sub>c</sub> (10 μM) in the absence or presence of Cat B (0.5 μg) in a PBS solution at 37 °C. (d and e) NIRF intensity versus time curves of the liver (d) and kidney (e) after injection of APN<sub>c</sub> in live mice (n = 4). (f) NIRF imaging of live mice with implanted tumours after APN<sub>c</sub> injection at different time points (0, 3, and 14 d). White circles display the tumour (T), liver (L), and kidney (K). (g) The correlation between the percentage of activated APN<sub>c</sub> in urine and tumour size was studied by linear regression analysis. (h) APN<sub>c</sub> was injected at different time points and the fluorescence intensity of the activated probe was collected in urine from each group of mice (n = 4). PBS versus tumour-implantation groups. Reproduced with permission from ref. 33. Copyright 2022, Springer Nature.

Besides, Kwon *et al.*<sup>36</sup> developed a novel exogenous administered activity-based tumour-penetrating nanosensor (ABN<sub>s</sub>) that can effectively detect tumour lesions  $< 5$  mm as well as micro nodes based on abnormal protease expression in the

tumour microenvironment (Fig. 4a). In the ABN<sub>s</sub> nanoplateform, Kwon *et al.* have chosen MMP9 as a protease target, modified with a tumour-penetrating peptide (LyP-1) to mediate the active internalization of ABN<sub>s</sub> and their transport

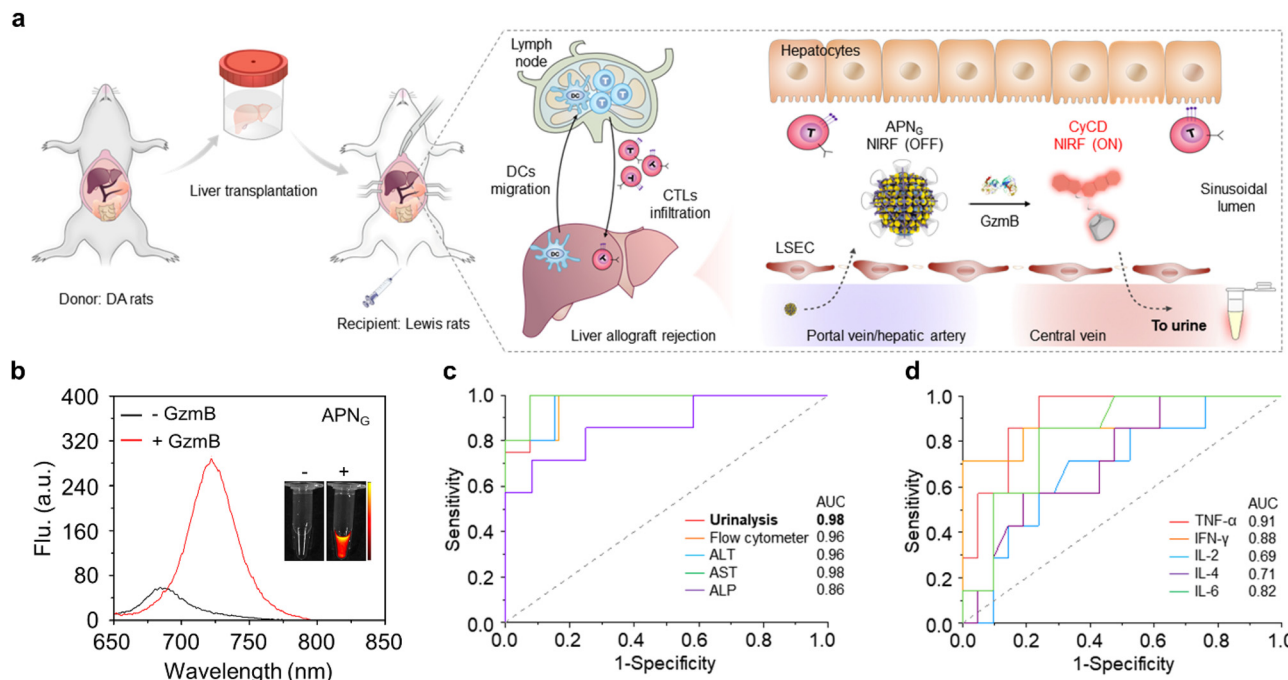


**Fig. 3** Urinalysis of acute liver allograft rejection in live rats. (a). Illustration of the liver transplantation surgical procedure, liver allograft rejection mechanisms, and APN<sub>G</sub> activation in the grafted liver for optical urinalysis in live mice. LSEC, liver sinusoidal endothelial cells. (b). NIR-fluorescence spectra of APN<sub>G</sub> in the absence or presence of granzyme B in a PBS solution at 37 °C. (c). Diagnostic specificity and sensitivity for urinalysis, flow cytometry, ALT, AST and ALP in differentiating between healthy rats ( $n = 12$ ) and allografts ( $n = 8$ ) 6 d after transplantation. (d). Diagnostic specificity and sensitivity for cytokines including TNF- $\alpha$ , IFN- $\gamma$ , IL-2, IL-4 and IL-6 in differentiating between healthy rats ( $n = 21$ ) and allografts ( $n = 14$ ) 6 d after transplantation. Reproduced with permission from ref. 33. Copyright 2022, Springer Nature.

through the tumour stroma into the tumour tissue, which significantly improved the sensitivity, as evidenced by detecting tumour sizes from 150 mm<sup>3</sup> to 30 mm<sup>3</sup> in volume. Furthermore, they selected another tumour penetrating peptide, iRGD, which is involved in the same active internalization pathway as LyP-1, but with an  $\alpha_1\beta_3$  or  $\alpha_1\beta_5$  integrin heterodimer as the central receptor. After intravenous (i.v.) administration, excellent tumour enrichment effects were observed in a mouse tumour model (Fig. 4b and c). Finally, in mice with tumours implanted for two weeks, the total tumour burden measured 36 mm<sup>3</sup>, with a median nodule diameter less than 2 mm. At this stage, urine test results show a notable increase in signals compared to the blood biomarker HE4 (Fig. 4b and e). When compared to clinically accepted imaging modalities capable of detecting only individual tumour nodules larger than 5 mm, the ABNs platform demonstrated greater sensitivity in the mouse model.

### 3. Detection of immune checkpoint blockade (ICB) responses

The advent of Immune Checkpoint Blockade (ICB) therapy has marked a significant progress in cancer treatment.<sup>37–39</sup> Nevertheless, it is important to note that objective response rates still fall below approximately 25% across several cancer types.<sup>38</sup> Currently, a combination of radiological assessments,

tumour evaluations, and serum biomarkers is employed to gauge patient responses to ICB therapy.<sup>40</sup> However, there is an evident need to enhance radiological evaluation following the initial cycle of ICB therapy, considering the occurrence of “pseudoprogression” during immunotherapy.<sup>41–45</sup> Furthermore, tumour biomarkers typically require invasive biopsy procedures during treatment, underscoring the critical importance of developing non-invasive assays for monitoring the immune response to ICB therapy.<sup>44</sup>

Kwong *et al.* have reported a category of active sensors as urinary biomarkers for assessing the ICB response.<sup>44</sup> These sensors comprise anti-programmed cell death protein 1 antibodies ( $\alpha$ PD1) in conjunction with fluorescently labelled, mass-coded protease substrates. Such substrates can be cleaved by proteases during ICB treatment, leading to the release of signal reporters that are subsequently filtered into the urine. Through urine sampling, both tumour and immuno-proteases can be quantified using fluorescence and mass spectrometry, allowing for the monitoring of ICB responses based on their distinctive mass barcodes. As a representative example, a fluorescently labelled peptide substrate that selectively targets murine granzyme B (GzmB; substrate IEFDSG<sup>46,47</sup>) was conjugated to an  $\alpha$ PD1 (clone 8H3) antibody *via* cross-linking surface amines on the antibody, resulting in the formation of an  $\alpha$ PD1-GzmB sensor conjugate, referred to as  $\alpha$ PD1-GS (Fig. 5a).

The capacity of  $\alpha$ PD1-GzmB sensor conjugates ( $\alpha$ PD1-GS) to detect the T cell-mediated killing of tumour cells was assessed

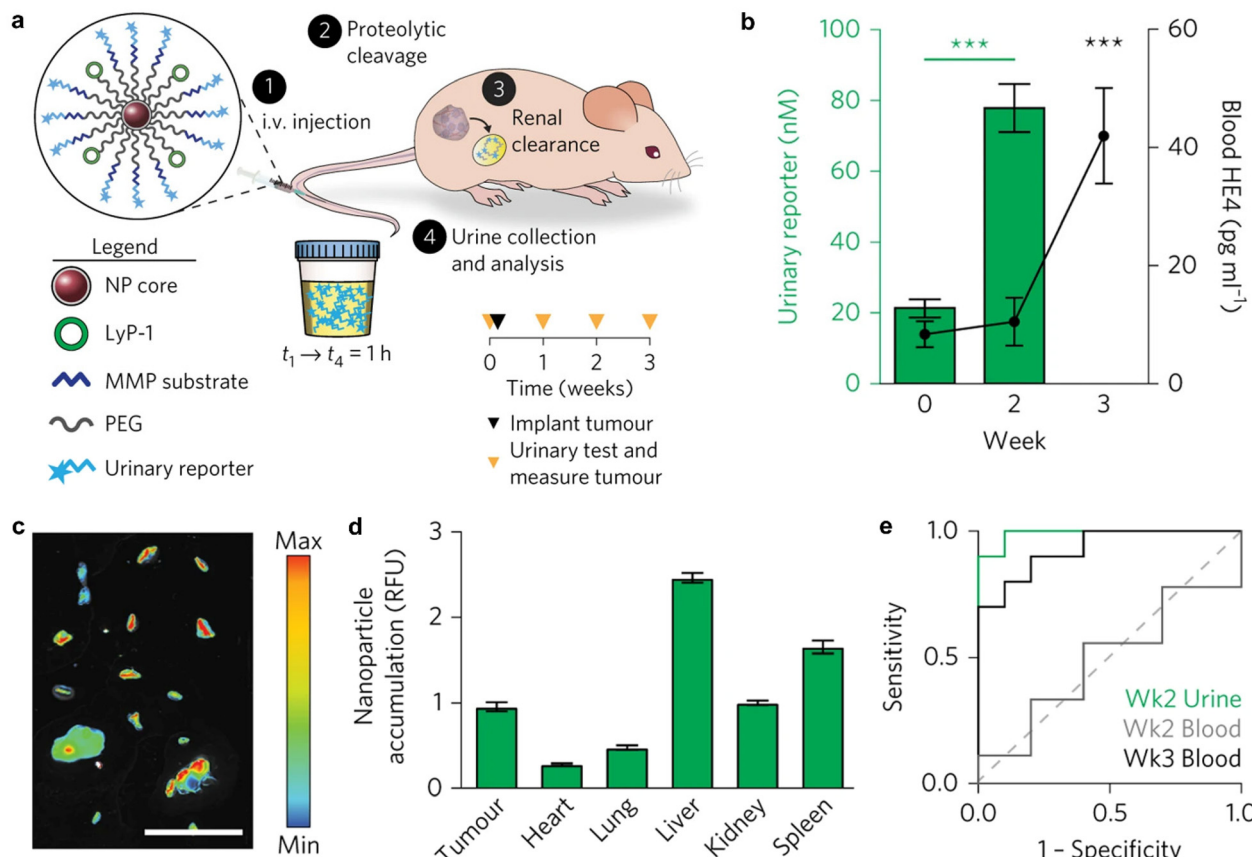


**Fig. 4** Tumour enrichment and urine detection mechanism of ABN<sub>S</sub>. (a). Illustration of the ABN<sub>S</sub> assembly and urine test pathway. (b). Urine and blood measurement of ABN<sub>S</sub> and HE4. (c). ABN<sub>S</sub> accumulation in tumour nodules in a representative animal. (d). Normalization accumulation of ABN<sub>S</sub> in tumours and major organs. (e). ROC curve of urinary diagnostic and blood biomarker. Reproduced with permission from ref. 36. Copyright 2017, Springer Nature.

in the MC38 colon adenocarcinoma syngeneic tumour model.<sup>48</sup> Following the administration of four doses of antibodies on days 7, 10, 14, and 17 to C57BL/6 mice bearing MC38 tumours, no statistically significant differences in tumour volume were observed between mice receiving  $\alpha$ PD1-GS and those administered with unmodified  $\alpha$ PD1. This corroborates that the coupling of the GzmB peptide does not affect the efficacy of ICB treatment. Subsequently, the capability of  $\alpha$ PD1-GS in monitoring the GzmB activity within a T cell killing assay was evaluated. The co-incubation of this conjugate with Pmel T cells and B16 tumour cells resulted in the separation of fluorescence reporter signals from internal busters and a subsequent increase in fluorescence levels in the samples. Conversely, no significant fluorescence increase was observed after incubating  $\alpha$ PD1-GS with fresh mouse serum, tumour-associated proteases (*e.g.*, histone B and MMP9), or coagulation and complement proteases (*e.g.*, C1s and thrombin) (Fig. 5b). This observation suggests that  $\alpha$ PD1-GS exhibits substrate-specificity during T cell killing and is particularly sensitive to GzmB activity. Finally, the non-invasive detection of  $\alpha$ PD1-GS response in C57BL/6 mice carrying homozygous MC38 tumours was evaluated. To ascertain whether  $\alpha$ PD1-GS

undergoes cleavage within tumours, a designed activatable probe containing a near-infrared fluorophore (800CW) and a quenching agent (QC1) was employed (Fig. 5d). When activated  $\alpha$ PD1-GS and Iso-GS were incubated with recombinant GzmB, the fluorescence intensity increased by ~1.5 and ~1.6 times, respectively (Fig. 5d). Mice bearing with MC38 tumours were injected with 2 doses of  $\alpha$ PD1 or isotype control antibodies, followed by the activation of  $\alpha$ PD1-GS or Iso-GS. There was no statistically significant difference in NIRF imaging of non-tumour organs (liver, spleen, dLNs (tumour draining lymph nodes), lung, kidney, heart, and brain), while NIR fluorescence in tumours was increased by 1.4 times (Fig. 5e and f), which suggested that  $\alpha$ PD1-GS accumulates in MC38 tumours and is cleaved to release enhanced fluorescence during ICB treatment. Following the treatment of MC38 tumours with  $\alpha$ PD1-GS or IgG1 isotype antibody conjugated to the GzmB peptide substrate (Iso-GS), representative flow cytometry plots revealed a significant increase in both the number and percentage of GzmB<sup>+</sup> tumour-infiltrating lymphocytes (TILs) within the CD3+CD8+ T cell subsets. However, there was no observable response of CD3+ CD8- subsets to  $\alpha$ PD1-GS compared to control mice receiving the same dose of Iso-GS, indicating that

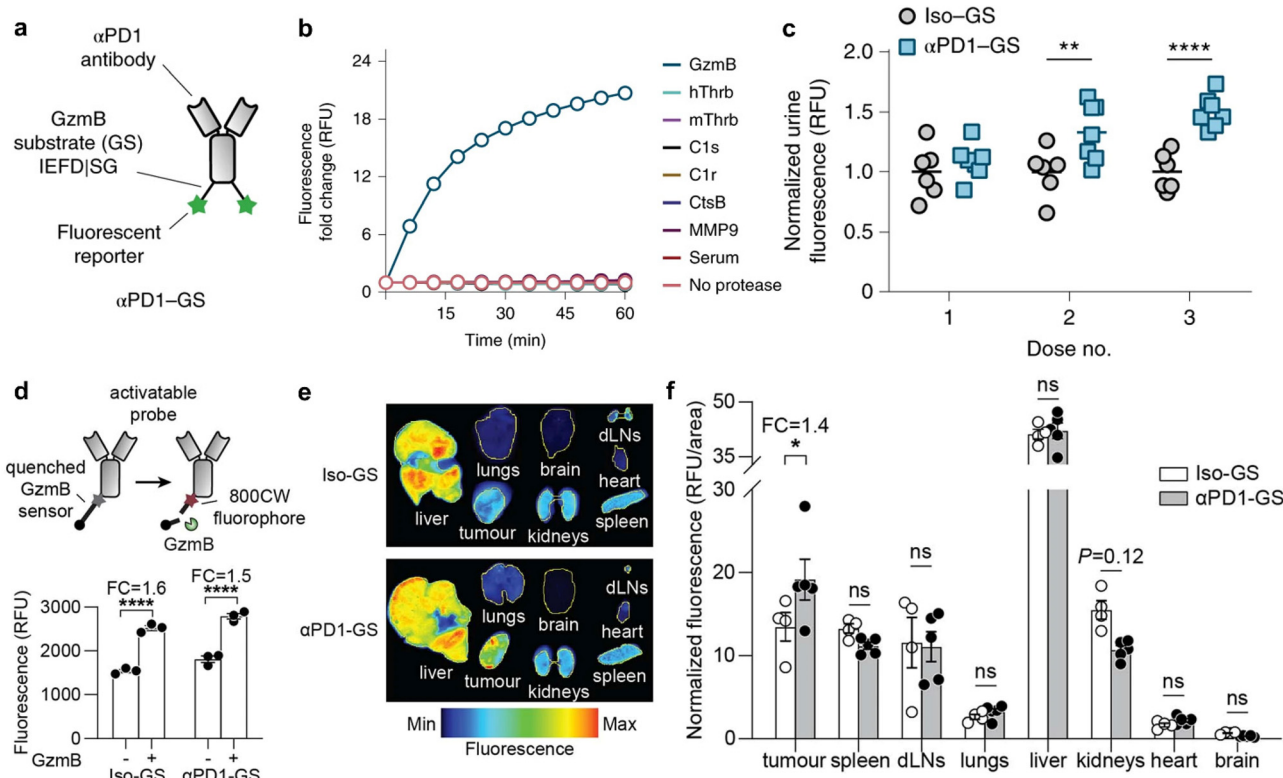


**Fig. 5** Assessment of ICB therapeutic response using antibody-GzmB sensor conjugates. (a) Schematic structure of the  $\alpha\text{PD1}$ -GzmB sensor conjugate ( $\alpha\text{PD1-GS}$ ). (b) Normalized fluorescence (relative fluorescence unit, RFU) of recombinant GzmB (blue), mouse serum (red) and other proteases incubated with  $\alpha\text{PD1-GS}$  ( $n = 3$ ). (c) Normalized urinary fluorescence of MC38 tumour-bearing mice after treatment with  $\alpha\text{PD1-GS}$  or Iso-GS ( $n = 6$ –7). (d) Schematic of the  $\alpha\text{PD1}$ -GzmB probe labelled with a quencher and a near-infrared fluorophore 800CW and fluorescence obtained by cleavage *in vitro* (FC, fold change;  $n = 3$ ) (e and f). Fluorescence images and quantitative analyses of tumour/non-tumour organs after treatment with Iso-GS or  $\alpha\text{PD1-GS}$  ( $n = 4$ –5). Reproduced with permission from ref. 44. Copyright 2022, Springer Nature.

CD8<sup>+</sup> TILs are the responsive cells to ICB treatment in this model.

To gauge the potential for continuous monitoring of the response to ICB treatment, two groups of MC38 tumour-bearing mice received treatment with either  $\alpha\text{PD1-GS}$  or Iso-GS. The concentration of cleaved fluorescent reporter signals in urine samples was quantified within 3 hours of administration on days 7, 10, and 14 (Fig. 5c). Compared to the control mice treated with Iso-GS, there were no statistically significant differences in urinary fluorescence signals between the two groups after the first dose. However, at the initiation of the second dose on day 10, the  $\alpha\text{PD1-GS}$ -treated mice exhibited significantly higher urinary fluorescence signals ( $P = 0.0093$ ,  $n = 6$ –7) while maintaining statistically comparable tumour volumes ( $255 \text{ mm}^3$  vs.  $441 \text{ mm}^3$ ,  $P = 0.68$ ,  $n = 6$ –7). Furthermore, the disparity in urinary fluorescence signals was further accentuated at the outset of the third dose on day 14 ( $P < 0.0001$ ,  $n = 6$ –7), and tumour volume also showed a significant difference ( $P < 0.0001$ ,  $n = 6$ –7). Receiver operating characteristic (ROC) analysis of urine samples at the reporting level indicated an area under the curve (AUC) of 0.86 for dose 2 and 1.00 for dose 3. This demonstrates the ability to discern ICB responses with a high degree of sensitivity and specificity.

Furthermore, the effectively therapeutic response at the outset of the second dose within the first cycle of ICB treatment was manifested in a preclinical animal model.

#### 4. Early detection of hepatic ischemia-reperfusion injury

Hepatic ischemia-reperfusion injury (IRI) represents a significant complication associated with various clinical procedures including hepatectomy, transplantation, and trauma.<sup>49</sup> Oxidative stress serves as a key pathophysiological mechanism in the course of hepatic IRI, ultimately leading to cell death.<sup>50</sup> Recently, clinical diagnostic approaches for hepatic IRI involve plasma markers (serum ALT/AST) and histological assays. In addition, non-invasive imaging techniques such as CT, MRI, and PET are employed.<sup>51–53</sup> Nevertheless, these methods are primarily designed to identify late-stage liver function changes and prove ineffective in the early detection of molecular-level alterations associated with hepatic IRI.<sup>51–54</sup>

Huang *et al.* have developed an activatable polymeric nanoprobe, APN<sub>SO</sub>, for real-time NIRF imaging of hepatic IRI and remote urinalysis in the early stage.<sup>55</sup> APN<sub>SO</sub> is composed of

four functional blocks: a superoxide anion ( $O_2^-$ ) reactive moiety, a self-immolative linker, a caged fluorophore moiety and a renal clearance moiety. The fluorophore moieties are convergently connected with the self-immolative linkers to form the polymer backbone, which is conjugated by an  $O_2^-$ -cleavable trifluoromethanesulfonate group and grafted by a renal-clearance moiety HP $\beta$ CD (Fig. 6a). The amphiphilic properties of these polymers enable them to spontaneously assemble into nanoparticles in aqueous solutions, with an average dynamic size of 160 nm. APN<sub>SO</sub> is naturally non-fluorescent. In the presence of  $O_2^-$ , the trifluoromethanesulfonate groups are cleaved, triggering self-depolymerization of the APN<sub>SO</sub> backbone. This process releases a renal-excretable fluorescent fragment referred to as the "fluorescent artificial urine biomarker" (FAUB) (Fig. 6a), leading to a new peak at 700 nm in the absorption spectrum (Fig. 6c) and an 11-fold fluorescence enhancement at 720 nm (Fig. 6d). The nanoprobe also exhibits a low limit of detection of about  $10 \times 10^{-9}$  M towards  $O_2^-$ . APN<sub>SO</sub> exhibited superior liver-oriented accumu-

lation, which is probably due to its large particle size of  $\sim 160$  nm that exceeded the renal filtration threshold of  $\sim 5$  nm (Fig. 6b). Despite high accumulation in the liver, APN<sub>SO</sub> exhibited only a weak background signal in healthy mice as it was intrinsically non-fluorescent.

The ability of APN<sub>SO</sub> to monitor hepatic IRI was tested in a mouse model of hepatic warm IRI.<sup>55,56</sup> APN<sub>SO</sub> was i.v. injected into live mice at various time points (0.25, 1, and 4 hours) after reperfusion. At 0.25 hours post reperfusion timepoint, the activated APN<sub>SO</sub> signal depicted both the liver and kidney in mice (Fig. 6g and h). In comparison, the maximal NIRF signals in the liver (and kidneys) of mice at 1 and 4 hours of reperfusion were 1.8 times (1.9 times) and 2.56 times (2.52 times), respectively (Fig. 6e and f). No significant differences in NIRF signals were observed in the NAC-pretreated group<sup>57</sup> when compared to the control group (Fig. 6e and f). In comparison of clinical diagnostic methods, it was observed that serum ALT and AST did not exhibit statistical elevation until 8 hours after reperfusion. This suggests that ALT and AST

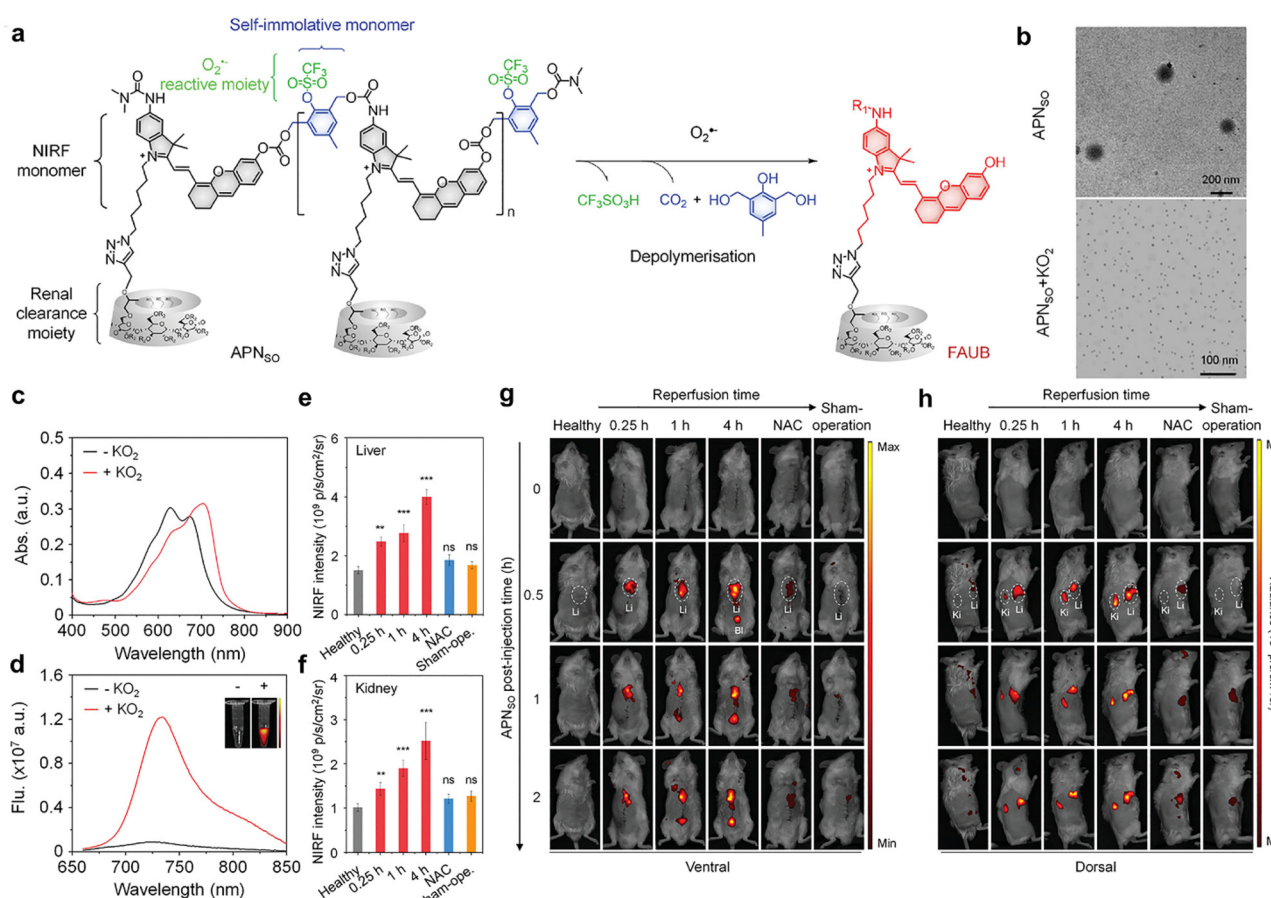


**Fig. 6** APN<sub>SO</sub>-based NIRF imaging and urinalysis of hepatic IRI. (a) Chemical structures of APN<sub>SO</sub> and its fluorescent fragment FAUB in the presence of  $O_2^-$ . ( $R_1 = H$  or  $(CH_3)_2NCO$ ,  $R_2 = H$  or  $CH_2CHOHCH_3$ ). (b) TME images of APN<sub>SO</sub> in a PBS solution before and after exposure to  $KO_2$  at 37 °C. Inset: Fluorescence images at 720 nm. (c and d) Absorption and fluorescence spectra of APN<sub>SO</sub> in a PBS solution before and after exposure to  $KO_2$  at 37 °C. Inset: Fluorescence images at 675 nm. (e and f) NIRF intensities of the liver and kidney of live mice with injection of APN<sub>SO</sub> at 0.5 h after different postreperfusion time points ( $n = 4$ ). (g and h) NIRF images of live mice with injection of APN<sub>SO</sub> at different time points after reperfusion for 0.25, 1, or 4 h. Reproduced with permission from ref. 55. Copyright 2022, John Wiley and Sons.

serve as insensitive later indicators for monitoring the liver function in the mouse model of hepatic IRI. Moreover, hepatic IRI was remotely detected by urinalysis. Following i.v. injection of APN<sub>SO</sub>, the fluorescence signal of FAUB in urine was measured at 1 hour, 4 hours, and 8 hours post reperfusion, respectively. Statistically significant enhancements in NIRF signals of FAUB were observed at 1 hour (1.93-fold) post reperfusion. Furthermore, the contrasting NIRF signals of FAUB continued to exhibit enhancement at 4 hours (3.02-fold) and 8 hours (6.11-fold) post reperfusion. Histological studies revealed normal liver tissue morphology at 4 hours post reperfusion, while significant necrosis was observed at 8 hours post reperfusion. Therefore, APN<sub>SO</sub>-based imaging and urinalysis can detect hepatic IRI up to 7 hours earlier than clinical serological biomarkers (ALT/AST) and histological analyses.

## 5. Diagnosis of thrombosis and inflammation

Postoperative infection and thromboembolism are life-threatening complications in clinical settings and are responsible

for high mortality annually worldwide.<sup>58</sup> Currently, the levels of prothrombin fragment 1.2 and D-dimer that serve as indicators of thrombosis or genetic tests have been used for monitoring pathogenic infections for patients in hospitals.<sup>58</sup> However, these indicators are often rapidly depleted in the bloodstream,<sup>59</sup> which makes them unable to capture signals associated with long-lasting latent diseases after the patient's discharge.

Bhatia *et al.*<sup>60</sup> have constructed synthetic biomarkers for diagnosis of thrombosis and infection. These synthetic biomarkers comprised three components: poly(ethylene glycol) (PEG) with a molecular weight of 40 kDa, thrombin or matrix metalloproteinase (MMP9) cleavable peptide linkers, and a urinary reporter, which acted as the core scaffold, surface linker and signal moiety, respectively (Fig. 7a).

After incubation with recombinant thrombin, significant fluorescence enhancement was observed within a short period of time, whereas PEG-conjugated peptide (PEG-T1Q) was negligibly cleaved by clotting cascade protease factor IX (Fig. 7b). In a parallel characterization study, remarkable fluorescence enhancement was observed after coincubation of PEG-M1Q with MMP9. However, negligible enhancements in fluo-

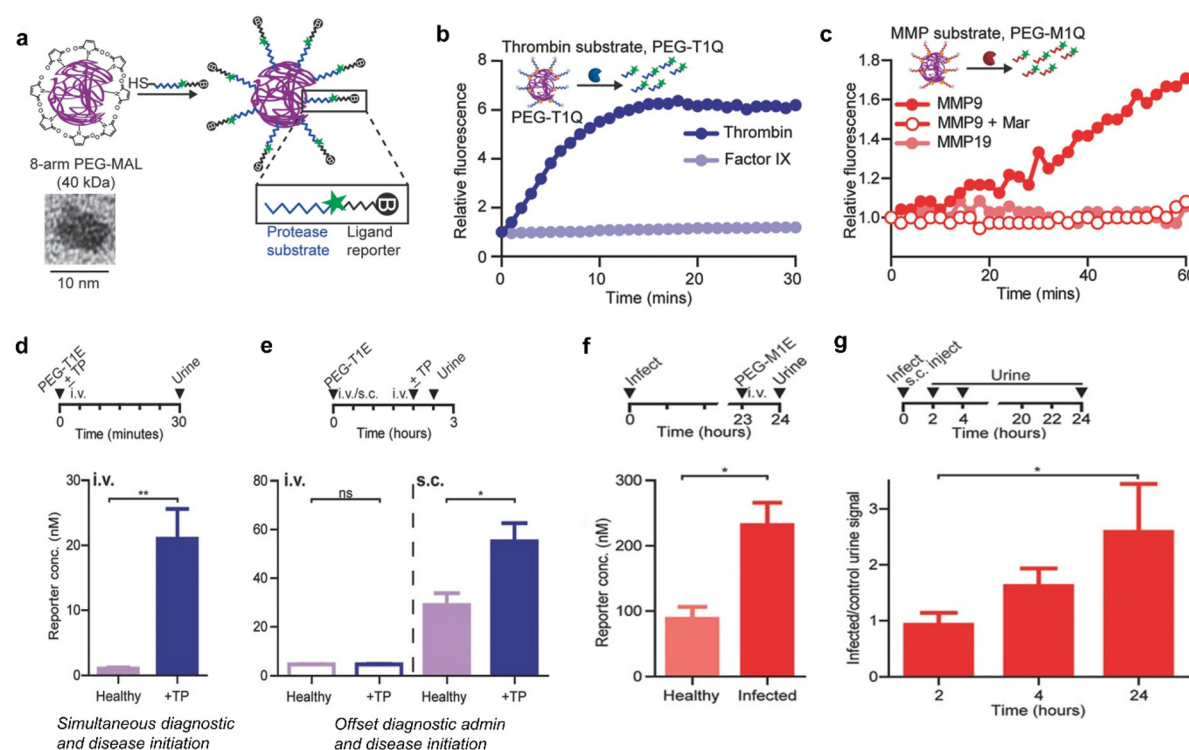


**Fig. 7** Diagnosis of thrombosis and inflammation using synthetic biomarkers. (a) Eight-arm PEG maleimide (PEG-MAL) reacts with peptides terminated with cysteine, which include urinary reporters and protease substrates. The inset shows a TEM image of the 40 kDa PEG molecule. (b) Representative dequenching measurements of PEG-T1Q (thrombin substrate) in the presence of recombinant thrombin, Factor IX. (c) Representative dequenching measurements of PEG-M1Q (MMP9 substrate) in the presence of MMPs; MMP9 inhibit Marimastat. (d) Diagnostically administered at the same time as the onset of disease in mice, PEG-T1E was effective in differentiating healthy mice from thrombosed mice. (e) There was no significant difference between diseased and healthy mice when administered intravenously prior to the onset of disease, whereas subcutaneous injection allowed diagnosis of pre-diseased mice. (f) *P. aeruginosa* was injected into the mouse lungs to establish an inflammation model, and 24 h later, PEG-M1E was administered intravenously, showing sensitivity to infection detection. (g) Subcutaneous injection of PEG-M1E detects later inflammation within 24 h. (I.D. = 4000 pmoles,  $n = 4-5$ ;  $\pm$ SEM). Reproduced with permission from ref. 60. Copyright 2016, John Wiley and Sons.

rescence signals were determined for the distinct enzyme MMP19 and pretreated with an MMP9 inhibitor Marimastat (Fig. 7c).

The ability of PEG-T1E to detect ongoing thrombosis was tested using a mouse model of thrombosis. After i.v. injection of thromboplastin and PEG-T1E, blood clots, primarily in the lung vasculature, were formed *via* the extrinsic clotting cascade. In addition, the urinary signal was significantly elevated related to healthy controls (Fig. 7d). However, such model did not mimic the kinetics of the onset of a postoperative complication in clinical settings, because the realistic postoperative complication is more likely to be delayed relative to the time of diagnostic administration. As such, subcutaneous administration of PEG-T1E was employed to read out a response to thromboplastin. The results indicated that the same dose of PEG-T1E administered subcutaneously 2 hours prior to disease onset allowed us to clearly distinguish between diseased and healthy animals (Fig. 7e). Furthermore,

the capability of the MMP-responsive synthetic biomarker (PEG-M1E) to detect inflammation associated with pneumonia was evaluated. In the course of infection, MMP9 is highly expressed by neutrophils and other immune cells as key mediators in innate immunity and inflammation. Followed by 24 hours post-intratracheal inoculation of *P. aeruginosa*, the urine reporter levels measured were significantly higher in infected mice compared to healthy controls after 1 hour i.v. injection of PEG-M1E (Fig. 7f). Finally, the PEG-M1E nanoprobe was subcutaneously injected to cohorts of mice that were either coinfect or not infected *via* pulmonary delivery of bacteria. The levels of urine reporter were measured periodically in both groups over a 24-hour period. In the initial period of 2 hours post injection, no difference between healthy and infected mice was observed. However, the urine signal in infected mice was significantly elevated at later time points from 2 to 24 hours due to the inflammatory response strengthened (Fig. 7g). Therefore, those synthetic biomarkers not only

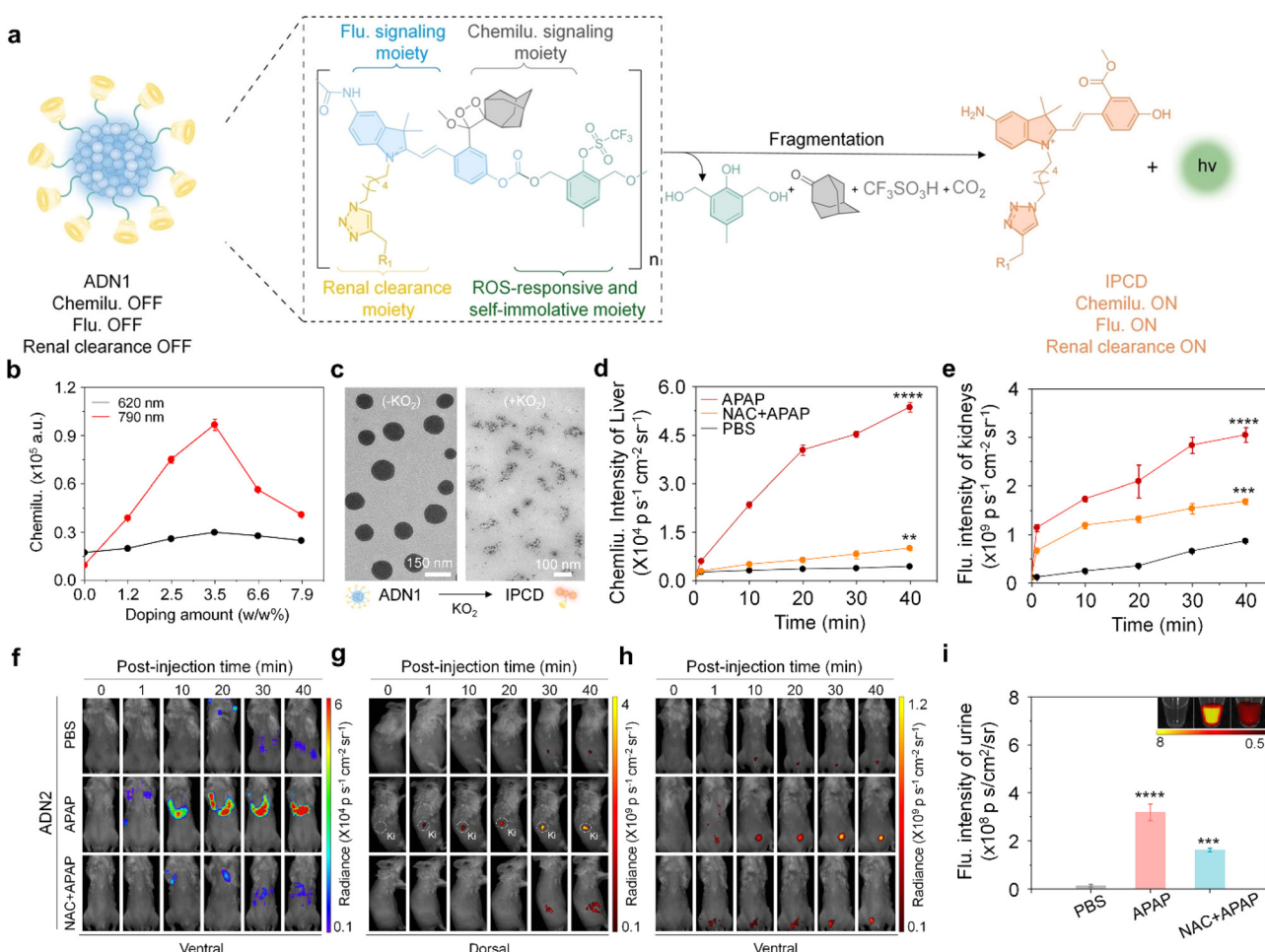


**Fig. 8** Duplex imaging and urinalysis of DILI using ADN2. (a) Chemical structure of ADN1 and its O<sub>2</sub><sup>-</sup> activated fragments (R<sub>1</sub> = HPβCD). (b) Doping content of the NCBS dye as a function of the chemiluminescence intensity of ADN2 in the presence of KO<sub>2</sub> (80 μM) at 620 nm and 790 nm. (c) Representative TEM images of ADN1 in the absence or presence of KO<sub>2</sub> in a PBS solution (similar size to ADN2). (d and e) Chemiluminescence intensities versus time curves of the liver (d) and kidney (e) after injection of ADN2 in live mice. (f–h) Chemiluminescence and fluorescence imaging of live mice after the injection of ADN2 at different time points. (i) The fluorescence intensities of excreted IPCD in the urine from live mice after intravenous injection of APN2 for 3 hours. Reproduced with permission from ref. 63. Copyright 2023, John Wiley and Sons.

enable long-term monitoring of diseases with facile urinary readouts, but also have high potentials for further advancement in monitoring and diagnostic applications in human.

## 6. Early detection of drug-induced liver injury

Drug-induced liver injury (DILI) poses a significant global public health concern.<sup>61</sup> Excessive exposure to hepatotoxic drugs can deplete glutathione, leading to the formation of toxic protein adducts, thereby increasing oxidative stress and ultimately resulting in liver injury.<sup>62</sup> Conventional methods relying on the measurement of ALT/AST levels and histological analyses have limitations in terms of their low sensitivity and specificity.

To tackle those issues, Huang *et al.* have recently reported an activatable nanoreporter, ADN2, with superoxide anion ( $O_2^{*-}$ )-triggered size transformation and chemo-fluoro-luminescence response for crosstalk-free duplex imaging of DILI and *in vitro* urinalysis (Fig. 8a).<sup>63</sup> ADN2 was prepared *via* co-nano-precipitation of NIR naphthalocyanine NCBS with ADN1, which comprised four functional components: a cascade self-eliminating moiety responsive to superoxide anions, a chemiluminescent signaling moiety (adamantyl-1,2-dioxane), a fluorescent signaling moiety, and a renal-clearable moiety (HP $\beta$ CD). These synthesized polymers could spontaneously form nanoparticles in an aqueous solution with an average diameter of ~130 nm (Fig. 8c). ADN2 was initially non-fluorescent and non-chemiluminescent as the phenol group was caged. In the presence of  $O_2^{*-}$ , the chemiluminescence signals gradually elevated with the increase in the doping weight percentage of NCBS, eventually saturating at 3.5% and decreasing at higher doping ratios (Fig. 8b). This was ascribed to a cascade self-elimination reaction and depolymerization of the polymer backbone occurred, leading to the release of renal-cleared fluorescent fragments (IPCDs) (Fig. 8a). This activation switched on both chemo-fluorescence channels, enabling crosstalk-free imaging and urinalysis.

The feasibility of ADN2 for real-time duplex imaging and urinalysis of DILI was conducted in a mouse model of Acetaminophen (APAP)-induced hepatotoxicity.<sup>62,64</sup> After injection of ADN2, the earliest time-point of the first statistically significant chemiluminescence signal increase in the liver was observed at 10 min, and gradually increased at later imaging time points for APAP-treated mice, but not for the control mice (Fig. 8d and e). The signal was 15.3-fold higher than that of the control mice at 40 min post-injection of ADN2, indicating the upregulation of  $O_2^{*-}$  during the progression of hepatotoxicity. In addition, kidney and bladder were delineated at 10 min post-injection of ADN2. Moreover, similarly gradual increased fluorescence signals in the kidney and bladder were observed (Fig. 8e–h). These results validated the sequential depolymerization of ADN2 and excretion of IPCD from the liver to kidneys. However, both chemiluminescence and fluorescence signals were attenuated in the liver, kidney and

bladder for NAC-treated mice. The SBR of chemiluminescence imaging was 5.2-fold higher than that of fluorescence imaging at 40 min post-injection of ADN2 in the liver of APAP-treated mice, implying that chemiluminescence had a higher sensitivity than that of fluorescence for liver imaging.

Moreover, the signals of urinary IPCD were measured after 3 hours of ADN2 injection. The fluorescence signals increased 16-fold and 1.3-fold for APAP-treated mice relative to the control mice and NAC-pretreated mice (Fig. 8i), respectively, validating ADN2-based urinalysis-enabled detection of hepatotoxicity. H&E staining showed normal hepatic morphology at 0.5 hours post treatment of APAP, but tissue necrosis at 6 hours post treatment. Through the comparison of ADN2-based duplex imaging/urinalysis and plasma/histological assays, ADN2-based duplex imaging/urinalysis possesses the superiority for early and sensitive detection of hepatotoxicity.

## 7. Conclusions

A substantial barrier facing early diagnosis of diseases using optical nanoprobes is the shallow tissue penetration depth due to high photon absorption and light scattering. To realize the diagnosis of deep tissue diseases, optical probes with degradable parameter, renal clearance and fluorescence activation are of high demand. Although various small molecular probes are reported for real-time optical imaging of various biomarkers for disease detection, their hepatobiliary clearance features impeded the feasibility of *in vitro* urinary detection.<sup>65–67</sup> In contrast, activatable nanoprobes are activated by abnormal disease-associated biomarkers, and initiate a pharmacokinetic switch by undergoing degradation and eventually releasing signal reporters into urine, for simple imaging and sensitive optical urinalysis. These intrinsic advantages coupled with *in vitro* detection have enabled real-time ultrasensitive detection of pathological biomarkers (*e.g.*, ROS and enzymes), physiological indexes (*e.g.*, pH and hypoxia), *etc.* Although various renal-clearable nanoprobes have been constructed recently, this field is still in the early stage. Challenges and opportunities coexist, and several issues are to be tackled. First, owing to the challenges in nanoprobe design, very few renal clearable nanoprobes for optical imaging have been reported, making a major roadblock to explore their further applications. Although some inorganic renal-clearable nanoprobes have been designed, they simply rely on the surface anchor *via* noncovalent bonds, and the used heavy metals failed to be completely degraded. Furthermore, their instability in physiological environments and long-term safety remain yet to be addressed. Therefore, more efforts should be devoted to design novel and highly biocompatible and biodegradable materials for constructing renal-clearable nanoprobes. Second, existing renal-clearable nanoprobes suffer from low targeting ability. The resulting severe off-target signals significantly compromise the accuracy of diagnosis. As such, novel nanoprobes with high targeting capability are highly needed. Clinical approved antibodies can be selected

and conjugated onto nanoprobe. Third, the luminescence of current renal-clearable optical nanoprobe is limited in the NIR-I window. Therefore, great efforts should be devoted to the construction of nanoprobe with the emission above 900 nm. Such improvements allow us to apply those nanoprobe in deeper seated diseases. Fourth, as the field is in its infancy, future clinical application has yet to proceed to pivotal trials to determine their use for disease diagnosis. Alternatively, as biomarkers are released from disease sites to circulation, efforts can be made to detect biomarkers *via* analysis of blood and other biofluids using nanoprobe. Through discussion, we hope to encourage the development of different optical probe platforms and hardware systems, obtaining high sensitivity and high selectivity in targeting tissues, thereby achieving early diagnosis and treatment of diseases.

## Conflicts of interest

There are no conflicts to declare.

## Acknowledgements

J. H. thanks the National Key R&D Program of China (2022YFA0912700), National Natural Science Foundation of China (22207130), the Key Research and Development Plan of Guangzhou City (202206080007), the Sun Yat-sen University Funded Program (2022\_76220\_B21127), the Fundamental Research Funds for the Central Universities (22lgqb35), the Introduced Innovative R&D Team Project of “The Pearl River Talent Recruitment Program” (2021ZT09Y544), Guangdong-H0.5songkong-Macao Research Team Project of the Guangdong Basic and Applied Basic Research Foundation (2022b1515130008) for the financial support. J. H. acknowledges the award of “The Recruitment Program of Global Youth Experts” and the support from the start-up funding of Sun Yat-Sen University. W. X. thanks the Fundamental Research Funds for the Central Universities, Sun Yat-sen University (No. 23qnpv119). W. G. H. thanks the National Natural Science Foundation of China (22275193), the Natural Science Foundation of Fujian Province (2021J06034), Self-Deployment Project Research Program of Haixi Institutes, Chinese Academy of Science, CXZX-2022-GH09 (E255KF0101), Fujian Institute of Research on the Structure of Matter, Chinese Academy of Sciences (E055AJ01).

## References

- V. Ntziachristos, J. Ripoll, L. H. V. Wang and R. Weissleder, *Nat. Biotechnol.*, 2005, **23**, 313–320.
- A. V. Naumova, M. Modo, A. Moore, C. E. Murry and J. A. Frank, *Nat. Biotechnol.*, 2014, **32**, 804–818.
- P. Cheng and K. Pu, *Nat. Rev. Mater.*, 2021, **6**, 1095–1113.
- G. Hong, A. L. Antaris and H. Dai, *Nat. Biomed. Eng.*, 2017, **1**, 0010.
- D. Yu, M. A. Baird, J. R. Allen, E. S. Howe, M. P. Klassen, A. Reade, K. Makhijani, Y. Song, S. Liu, Z. Murthy, S.-Q. Zhang, O. D. Weiner, T. B. Kornberg, Y.-N. Jan, M. W. Davidson and X. Shul, *Nat. Methods*, 2015, **12**, 763–765.
- S. Roy, N. Bag, S. Bardhan, I. Hasan and B. Guo, *Adv. Drug Delivery Rev.*, 2023, **190**, 114821.
- L. Zhang, Y. Liu, H. Huang, H. Xie, B. Zhang, W. Xia and B. Guo, *Adv. Drug Delivery Rev.*, 2022, **190**, 114536.
- C. L. Walsh, P. Tafforeau, W. L. Wagner, D. J. Jafree, A. Bellier, C. Werlein, M. P. Kuhnle, E. Boller, S. Walker-Samuel, J. L. Robertus, D. A. Long, J. Jacob, S. Marussi, E. Brown, N. Holroyd, D. D. Jonigk, M. Ackermann and P. D. Lee, *Nat. Methods*, 2021, **18**, 1532–1541.
- J. Schwenck, D. Sonanini, J. M. Cotton, H.-G. Rammensee, C. la Fougere, L. Zender and B. J. Pichler, *Nat. Rev. Cancer*, 2023, **23**, 474–490.
- P. J. Keall, C. Brighi, C. Glide-Hurst, G. Liney, P. Z. Y. Liu, S. Lydiard, C. Paganelli, P. Trang, S. Shan, A. C. Tree, U. A. van der Heide, D. E. J. Waddington and B. Whelan, *Nat. Rev. Clin. Oncol.*, 2022, **19**, 458–470.
- S. Vilov, B. Arnal, E. Hojman, Y. C. Eldar, O. Katz and E. Bossy, *Sci. Rep.*, 2020, **10**, 4637.
- M. J. Schnermann, *Nature*, 2017, **551**, 176–177.
- L. Wu, J. Huang, K. Pu and T. D. James, *Nat. Rev. Chem.*, 2021, **5**, 406–421.
- J. Huang, C. Xie, X. Zhang, Y. Jiang, J. Li, Q. Fan and K. Pu, *Angew. Chem., Int. Ed.*, 2019, **58**, 15120–15127.
- J. Huang and K. Pu, *Chem. Sci.*, 2021, **12**, 3379–3392.
- J. Huang, J. Li, Y. Lyu, Q. Miao and K. Pu, *Nat. Mater.*, 2019, **18**, 1133–1143.
- B. You, Y. Zhang, Y. Jiao, K. Davey and S. Z. Qiao, *Angew. Chem., Int. Ed.*, 2019, **58**, 11796–11800.
- A. L. Vahrmeijer, M. Hutteman, J. R. van der Vorst, C. J. H. van de Velde and J. V. Frangioni, *Nat. Rev. Clin. Oncol.*, 2013, **10**, 507–518.
- N. Nishio, N. S. van den Berg, S. van Keulen, B. A. Martin, S. Fakurnejad, N. Teraphongphom, S. U. Chirita, N. J. Oberhelman, G. Lu, C. E. Horton, M. J. Kaplan, V. Divi, A. D. Colevas and E. L. Rosenthal, *Nat. Commun.*, 2019, **10**, 5044.
- J. G. Huang, Y. Y. Jiang, J. C. Li, S. S. He, J. S. Huang and K. Y. Pu, *Angew. Chem., Int. Ed.*, 2020, **59**, 4415–4420.
- S. S. He, J. C. Li, Y. Lyu, J. G. Huang and K. Y. Pu, *J. Am. Chem. Soc.*, 2020, **142**, 7075–7082.
- J. G. Huang, J. C. Li, Y. Lyu, Q. Q. Miao and K. Pu, *Nat. Mater.*, 2019, **18**, 1133–1143.
- K. S. de Valk, H. J. Handgraaf, M. M. Dekken, B. G. S. Mulder, A. R. Valentijn, A. G. T. van Scheltinga, J. Kuil, M. J. van Esdonk, J. Vuijk, R. F. Bevers, K. C. Peeters, F. A. Holman, J. V. Frangioni, J. Burggraaf and A. L. Vahrmeijer, *Nat. Commun.*, 2019, **10**, 3118.
- R. Tian, Q. Zeng, S. Zhu, J. Lau, S. Chandra, R. Ertsey, K. S. Hettie, T. Teraphongphom, Z. Hu, G. Niu, D. O. Kiesewetter, H. Sun, X. Zhang, A. L. Antaris, B. R. Brooks and X. Chen, *Sci. Adv.*, 2019, **5**, eaaw0672.

- 25 J. F. Lovell, C. S. Jin, E. Huynh, H. Jin, C. Kim, J. L. Rubinstein, W. C. W. Chan, W. Cao, L. V. Wang and G. Zheng, *Nat. Mater.*, 2011, **10**, 324–332.
- 26 Q. Miao, C. Xie, X. Zhen, Y. Lyu, H. Duan, X. Liu, J. V. Jokerst and K. Pu, *Nat. Biotechnol.*, 2017, **35**, 1102–1110.
- 27 H. S. Choi, W. Liu, P. Misra, E. Tanaka, J. P. Zimmer, B. I. Ipe, M. G. Bawendi and J. V. Frangioni, *Nat. Biotechnol.*, 2007, **25**, 1165–1170.
- 28 B. Du, X. Jiang, A. Das, Q. Zhou, M. Yu, R. Jin and J. Zheng, *Nat. Nanotechnol.*, 2017, **12**, 1096–1102.
- 29 W. Poon, Y.-N. Zhang, B. Ouyang, B. R. Kingston, J. L. Y. Wu, S. Wilhelm and W. C. W. Chan, *ACS Nano*, 2019, **13**, 5785–5798.
- 30 C. N. Loynachan, A. P. Soleimany, J. S. Dudani, Y. Lin, A. Najer, A. Bekdemir, Q. Chen, S. N. Bhatia and M. M. Stevens, *Nat. Nanotechnol.*, 2019, **14**, 883–890.
- 31 X. Jiang, B. Du and J. Zheng, *Nat. Nanotechnol.*, 2019, **14**, 874–882.
- 32 S. D. Perrault and W. C. W. Chan, *Proc. Natl. Acad. Sci. U. S. A.*, 2010, **107**, 11194–11199.
- 33 J. Huang, X. Chen, Y. Jiang, C. Zhang, S. He, H. Wang and K. Pu, *Nat. Mater.*, 2022, **21**, 598–607.
- 34 J. Huang, S. Weinfurter, P. C. Pinto, M. Pretze, B. Kraenzlin, J. Pill, R. Federica, R. Perciaccante, L. Della Ciana, R. Masereeuw and N. Gretz, *Bioconjugate Chem.*, 2016, **27**, 2513–2526.
- 35 J. Huang, S. Weinfurter, C. Daniele, R. Perciaccante, R. Federica, L. Della Ciana, J. Pill and N. Gretz, *Chem. Sci.*, 2017, **8**, 2652–2660.
- 36 E. J. Kwon, J. S. Dudani and S. N. Bhatia, *Nat. Biomed. Eng.*, 2017, **1**, 0054.
- 37 G. Morad, B. A. Helmink, P. Sharma and J. A. Wargo, *Cell*, 2021, **184**, 5309–5337.
- 38 A. Ribas and J. D. Wolchok, *Science*, 2018, **359**, 1350–1355.
- 39 P. Sharma and J. P. Allison, *Science*, 2015, **348**, 56–61.
- 40 M. Nishino, N. H. Ramaiya, H. Hatabu and F. S. Hodi, *Nat. Rev. Clin. Oncol.*, 2017, **14**, 655–668.
- 41 F. S. Hodi, W.-J. Hwu, R. Kefford, J. S. Weber, A. Daud, O. Hamid, A. Patnaik, A. Ribas, C. Robert, T. C. Gangadhar, A. M. Joshua, P. Hersey, R. Dronca, R. Joseph, D. Hille, D. Xue, X. N. Li, S. P. Kang, S. Ebbinghaus, A. Perrone and J. D. Wolchok, *J. Clin. Oncol.*, 2016, **34**, 1510–1517.
- 42 A. Vozy and G. Zaleman, *Oncologie*, 2015, **17**, 407–408.
- 43 M. Nishino, A. Giobbie-Hurder, M. P. Manos, N. Bailey, E. I. Buchbinder, P. A. Ott, N. H. Ramaiya and F. S. Hodi, *Clin. Cancer Res.*, 2017, **23**, 4671–4679.
- 44 Q. D. Mac, A. Sivakumar, H. Phuengkham, C. Xu, J. R. Bowen, F.-Y. Su, S. Z. Stentz, H. Sim, A. M. Harris, T. T. Li, P. Qiu and G. A. Kwong, *Nat. Biomed. Eng.*, 2022, **6**, 310–324.
- 45 M. Gerwing, K. Herrmann, A. Helfen, C. Schliemann, W. E. Berdel, M. Eisenblätter and M. Wildgruber, *Nat. Rev. Clin. Oncol.*, 2019, **16**, 442–458.
- 46 Q. D. Mac, D. V. Mathews, J. A. Kahla, C. M. Stoffers, O. M. Delmas, B. A. Holt, A. B. Adams and G. A. Kwong, *Nat. Biomed. Eng.*, 2019, **3**, 281–291.
- 47 L. Martinez-Lostao, A. Anel and J. Pardo, *Clin. Cancer Res.*, 2015, **21**, 5047–5056.
- 48 M. Efremova, D. Rieder, V. Klepsch, P. Charoentong, F. Finotello, H. Hackl, N. Hermann-Kleiter, M. Loewer, G. Baier, A. Krogsdam and Z. Trajanoski, *Nat. Commun.*, 2018, **9**, 32.
- 49 H. K. Eltzschig and T. Eckle, *Nat. Med.*, 2011, **17**, 1391–1401.
- 50 M. Cannistra, M. Ruggiero, A. Zullo, G. Gallelli, S. Serafini, M. Maria, A. Naso, R. Grande, R. Serra and B. Nardo, *Int. J. Surg.*, 2016, **33**, S57–S70.
- 51 M. Shoup, M. Gonan, M. D'Angelica, W. R. Jarnagin, R. P. DeMatteo, L. H. Schwartz, S. Tuorto, L. H. Blumgart and Y. M. Fong, *J. Gastrointest. Surg.*, 2003, **7**, 325–330.
- 52 W. de Graaf, R. J. Bennink, R. Vetelainen and T. M. van Gulik, *J. Nucl. Med.*, 2010, **51**, 742–752.
- 53 B. E. Van Beers, J.-L. Daire and P. Garteiser, *J. Hepatol.*, 2015, **62**, 690–700.
- 54 D. N. Granger and P. R. Kvietys, *Redox Biol.*, 2015, **6**, 524–551.
- 55 J. Huang, S. Xian, Y. Liu, X. Chen, K. Pu and H. Wang, *Adv. Mater.*, 2022, **34**, 2201357.
- 56 Y. Abe, I. N. Hines, G. Zibari, K. Pavlick, L. Gray, Y. Kitagawa and M. B. Grisham, *Free Radicals Biol. Med.*, 2009, **46**, 1–7.
- 57 H. Nakano, K. Boudjema, E. Alexandre, P. Imbs, M. P. Chenard, P. Wolf, J. Cinqualbre and D. Jaeck, *Hepatology*, 1995, **22**, 539–545.
- 58 M. F. Monn, X. Hui, B. D. Lau, M. Streiff, E. R. Haut, E. C. Wick, J. E. Efron and S. L. Gearhart, *Dis. Colon Rectum*, 2014, **57**, 497–505.
- 59 G. A. Kwong, S. Ghosh, L. Gamboa, C. Patriotis, S. Srivastava and S. N. Bhatia, *Nat. Rev. Cancer*, 2021, **21**, 655–668.
- 60 J. S. Dudani, C. G. Buss, R. T. K. Akana, G. A. Kwong and S. N. Bhatia, *Adv. Funct. Mater.*, 2016, **26**, 2919–2928.
- 61 W. Bernal, G. Auzinger, A. Dhawan and J. Wendon, *Lancet*, 2010, **376**, 190–201.
- 62 M. Yan, Y. Huo, S. Yin and H. Hu, *Redox Biol.*, 2018, **17**, 274–283.
- 63 B. Ruan, M. Yu, Y. Zhou, W. Xu, Y. Liu, B. Liu, L. Zhu, S. Yi, Y. Jiang and J. Huang, *Angew. Chem.*, 2023, **135**, e202305812.
- 64 C. Sheng, J. Zhao, Z. Di, Y. Huang, Y. Zhao and L. Li, *Nat. Biomed. Eng.*, 2022, **6**, 1074–1084.
- 65 J. J. Chen, L. Q. Chen, Y. L. Wu, Y. C. Fang, F. Zeng, S. Z. Wu and Y. L. Zhao, *Nat. Commun.*, 2021, **12**, 6870.
- 66 L. Y. Wu, Y. Ishigaki, Y. X. Hu, K. Sugimoto, W. H. Zeng, T. Harimoto, Y. D. Sun, J. He, T. Suzuki, X. Q. Jiang, H. Y. Chen and D. J. Ye, *Nat. Commun.*, 2020, **11**, 446.
- 67 J. H. Liu, W. Zhang, C. M. Zhou, M. M. Li, X. Wang, W. Zhang, Z. Z. Liu, L. L. Wu, T. D. James, P. Li and B. Tang, *J. Am. Chem. Soc.*, 2022, **144**, 13586–13599.